Novel hypothesis on the occurrence of sandbars

S. Seki,[1] D. Moteki,[1] and H. Yasuda[2, a)]

[1)]*Graduate School of Science and Technology, Niigata University, Niigata, Japan*

[2)]*Research Institute for Natural Hazards & Disaster Recovery Niigata University, Niigata, Japan*

(Dated: 11 August 2023)

The mechanism of sandbars initiation and formation is unresolved. The occurrence of sandbars has been investigated using stability analysis, which assumes that sandbars occur due to the inherent instability of a riverbed. However, there are no data, either from riverine observations or model experiments, to support this assumption. Here, we conducted flume experiments in which sandbars were formed from a flatbed by simultaneously measuring the water surface and bottom surface. The results showed that the process of sandbars initiation and formation first involves the generation of small periodic bedforms; then, the bedforms transition to small three-dimensionally shaped rhomboid bars, and finally the rhomboid bars transition to sandbars. The measurements also suggested that wave trains occurred on the water surface. We then conducted fixed-bed experiments under the same conditions as a moving bed to ascertain the behavior of the water surface. The results of these fixed-bed experiments showed that standing waves were observed on the water surface even when the experimental conditions were steady and the flatbed channel was straight. A two-dimensional wavenumber analysis showed that the dominant wavenumbers of the standing waves and initial small bedforms were in good agreement. The whole set of results indicated that standing waves were already present on the water surface before bedforms occurred and that one of the factors in sandbars initiation was the presence of standing waves on the water surface.

[a)]Author to whom correspondence should be addressed :

hiro@gs.niigata-u.ac.jp

I. INTRODUCTION

The morphologies of river channels can be classified into three categories: braiding, meandering, and straight[1]. In all three channel categories, geometric shapes called sandbars can spontaneously form on a riverbed. Sandbars are three-dimensional (3D) shapes with alternating deposition and scouring in longitudinal and transverse directions. Considering this spontaneous periodic shape, sandbars formation can be attributed to self-assembly[2]. Knowing how and why sandbars form is a scientifically important subject that contributes to the elucidation of self-assembly in general.

Understanding the mechanism of sandbars formation has also engineering value as follows. A bar wavelength is several times larger than the channel width, and the bar height is scaled to the flow depth, causing the flow to meander. During floods, flow deflection becomes more pronounced, resulting in large-scale channel fluctuations. In a worst-case scenario, flowing water can breach embankments, thus flooding cities and causing extensive damage. For this reason, there is an urgent need to understand how sandbars spontaneously form.

Field observations of rivers have long been conducted to understand the mechanism of sandbars formation[1,3]. Recent studies have clarified various sandbars properties by measuring bedforms with multibeam sonar and flow velocities with acoustic Doppler current profilers (ADCP)[4] as well as elucidating sandbars responses from several years of observations[5,6]. Earlier this year, Branß, Aberle, and Hentschel[7] proposed a method for estimating sandbars characteristics based on statistically derived geometric parameters. However, river measurements are limited by spatial and temporal scale constraints, and it is difficult to understand sandbars behavior under a wide variety of conditions such as hydraulic parameters, sand supply, and channel geometry. Previous studies have thus used flume experiments, theoretical analysis, and numerical analysis as alternative methods.

Studies using laboratory flumes have proposed equations for estimating basic physical quantities such as bar wavelength, height, and celerity[8–10]. Studies have also been conducted to elucidate the origin of sandbars because understanding why sandbars occur is essential for explaining the mechanism of sandbars formation. A current finding showed that one of the origins of sandbars is multimodal 3D bedforms, which obliquely intersect a channel[11]. They are also called rhomboid bars[12], rhomboid beach patterns[13], and oblique dunes[14], but in this paper, we refer to these 3D bedforms as "rhomboid bars" following Ikeda[12]. Rhomboid bars may help initiate sandbars

because they occur early in the process of sandbars formation and have a 3D shape. However, rhomboid bars have relatively small wavelengths and heights, which fact makes them difficult to observe. Researchers have yet to establish a unified understanding of the mechanism by which rhomboid bars form from flatbeds[13], and our understanding of sandbars initiation is poor.

Theoretical methods using linear stability analysis have shown that conditions for the occurrence of sandbars depend on the width-to-depth ratio of a river channel[15–20]. This analysis also provides that the width-to-depth ratio is an indicator of whether the river channel is braiding or meandering[21]. In the analysis, the following sequence of processes is hypothesized for the occurrence of sandbars[17]. First, a small perturbation is introduced to the initial bed and hydraulic parameters. If the width-to-depth ratio β exceeds a critical value β_c here, the bottom perturbation changes the flow pattern and sediment transport. Then, the bottom perturbation develops through interaction with the flow. At this time, a mechanism that selects bottom wavenumbers engages, and sandbars are formed. However, there are currently no measurement data to substantiate this process, and how sandbars actually occur has not been explained.

Numerical studies have shown that placing obstacles such as humps or introducing small random perturbations to the initial bed are effective at reproducing the occurrence and development of sandbars[22–24]. It is also known that the initial bedforms in numerical analyses are similar to the rhomboid bars seen in flume experiments[25]. However, it remains to be proven how well the numerical results correspond to the actual physical mechanisms and formation processes, because there is no measurement method that can be compared with the processes described by numerical analyses.

Theoretical and numerical analyses assume that bottom instability causes sandbars. Conversely, a recent study[26] measured both the water surface and bottom surface during the sandbars formation process and then demonstrated that the water surface contributes more to the determination of the flow depth distribution than the bottom surface in the initial phase of sandbars formation. If the water surface fails to maintain a flat condition given initially before bedforms occur, the bottom instability may be caused by the water surface.

This study revisited the conventional hypothesis on the occurrence of sandbars. In Sec. II, we measured the process of sandbars formation at high density and high frequency in a laboratory flume and quantified the wavenumbers of the water surface and bottom surface. In Sec. III, we conducted flume experiments on a fixed bed and showed that standing waves existed on the water surface before the occurrence of small bedforms. In Sec. IV, we discussed what generates

the standing waves. In this section, we also proposed a novel hypothesis on the occurrence of sandbars. Finally, Sec. V provides a summary of this paper.

II. FLUME EXPERIMENT ON A MOVING BED

A. Experimental conditions

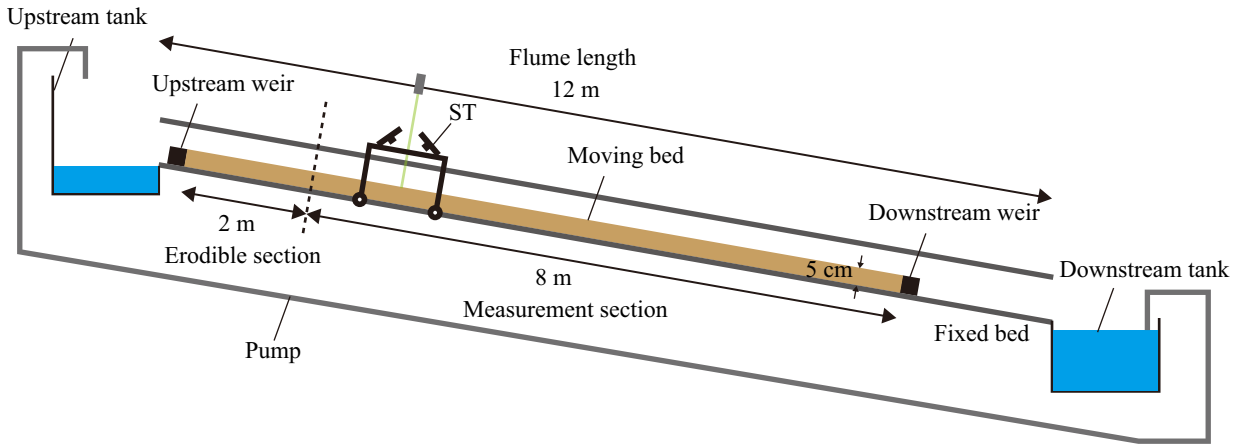

FIG. 1. Longitudinal view of flume in the moving bed experiment.

The channel used for the experiment is shown in Fig. 1. The flume was a straight rectangular section made of fiber reinforced plastic with a channel width B of 45 cm and a total length of 12 m. The length of the moving bed section was 10 m. The channel was constructed with 5 cm high weirs at the upstream and downstream ends of the moving bed section. In this experiment, the channel was given a flatbed of uniformly spread silica sand with an average grain size d of 0.76 mm as the initial condition. To minimize artificial influences on the occurrence of bedforms, a erosion zone of 2 m in length was placed at the upstream end of the channel. These are the so-called free bars conditions[27,28]. Water supply was provided from the upstream end, the flow rate Q was assumed to be steady, and an electromagnetic flow meter was used to confirm that the steady state was maintained.

In this experiment, the conditions for the formation of alternate bars were set based on the Kuroki and Kishi [15] classification diagram, with flow rate and channel slope I_0 as variables. The specific conditions are shown in Table I, where τ_{*0} and F_0 are the Shields number and Froude

TABLE I. Hydraulic conditions.

Case	β[-]	τ_{*0}[-]	F_0[-]	I_0[-]	Q[L/s]	$t_{\max}$[min]	$t^*_{\max}$[-]
1	23.9	0.075	1.05	1/100	1.35	80	21.2
2	14.3	0.063	0.81	1/200	2.25	240	22.4
3	20.5	0.029	0.62	1/300	1.00		
4	17.8	0.067	0.90	1/150	1.83		

number, respectively, assuming a uniform flow. β, τ_{*0}, and F_0 are given as follows:

$$\beta = \frac{B}{2h_0}, \tag{1}$$

$$\tau_{*0} = \frac{h_0 I_0}{sd}, \tag{2}$$

$$F_0 = \frac{u_0}{\sqrt{gh_0}}, \tag{3}$$

where h_0 is the uniform flow depth obtained from Manning's equation, s is the specific gravity of the sediments in the water, $s = 1.65$, g is the gravitational acceleration, $g = 9.81$ m/s^2, and u_0 is the uniform flow velocity. Manning's roughness coefficient $n = 0.014$ s/m$^{1/3}$ was used from the Manning Strickler equation to obtain the above parameters. The clear difference between the two cases is the time required for sandbars to reach a dynamic equilibrium state.

B. Measurement method

Stream tomography (ST)[29] was used as a measurement method to quantify the geometric relationship between the water surface and bottom surface. ST is capable of noncontact measurement of the water surface and bottom surface during the sandbars formation process. The measurements were conducted at 1-minute intervals until the sandbars reached a state of dynamic equilibrium. The experiments were terminated when the bar wavelength and height were visually constant. The specific experimental termination time $t_{\max}$ was 80 minutes in Case 1 and 240 minutes in Case 2. As shown in Table I, the dimensionless experimental termination time $t^*_{\max}$ agrees in the two cases. The dimensionless experimental time t^* is given as follows[20,25,30]:

$$t^* = t\frac{qs_0}{(1-p)h_0 B/2}, \tag{4}$$

$$qs_0 = 8(\tau_{*0} - \tau_{*c})^{3/2}\sqrt{sgd^3}, \tag{5}$$

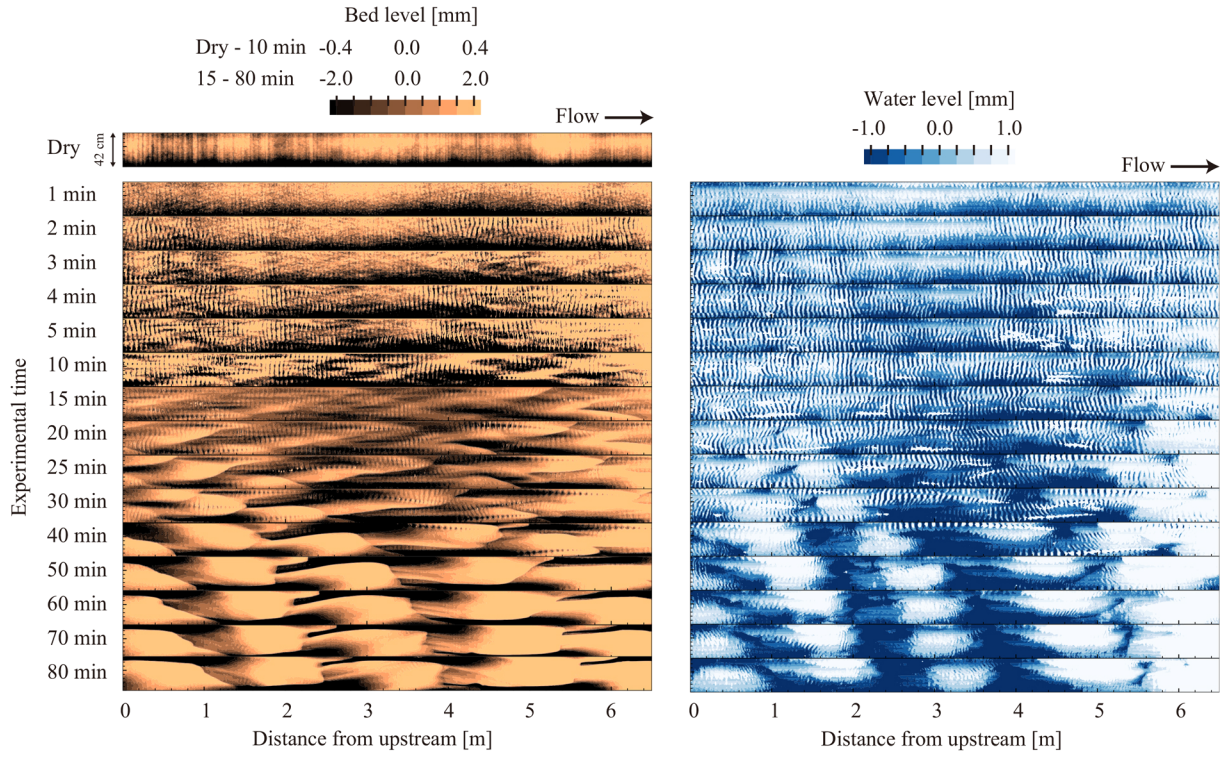

FIG. 2. Plane view of the dry bed level, the bed level and water level measured by ST under the condition of Member 3 in Case 1. The horizontal axis is the distance from the upstream of the measurement section. The vertical axis is the distance from the right bank. The coloring range of the bed level is different between Dry to 10 min and 15 min to 80 min from the beginning of the experiments.

$$\tau_{*c} = \frac{55.0d}{sgd} = 0.034, \tag{6}$$

where t is the experimental time, qs_0 is the sediment flux at uniform flow, p is the bed porosity, $p = 0.4$, and τ_{*c} is the critical Shields number[31]. The experiment was conducted five times under each condition.

C. Results

1. The sandbars formation process

Figs. 2 and 3 show the plane view of the bed level and water level measured by ST in Case 1 and Case 2, respectively. The channel width is shown only at 42 cm due to the measurement limitations of ST near the sidewalls. As described above, measurements were conducted at 1-minute intervals, but the intervals shown were adjusted for space constraints. Note that the range

of the bed level varies with time due to coloring.

The focus is on phenomena before and immediately after the water is supplied. Fig. 4 displays a limited section because the initial phenomenon is relatively small. Fig. 4 (left) shows that the initial bottom shape is flat. However, Fig. 4 (middle) shows that bottom undulations already occur 1 minute from the beginning of the experiments in both cases. The wavelength of the bottom undulations is approximately 5 cm. The shape of the water surface at the same time (Fig. 4 (right)) is similar to that of the bottom surface, and the wavelength of the water surface is also 5 cm. As seen in the legend, the wave height of the water surface is larger than that of the bedforms. This is also evident from the results of the 2D wavenumber analysis described below.

After 2 minutes from the beginning of the experiments in Figs. 2 and 3, wave heights gradually increased both at the bottom and water surfaces. According to previous studies, the bedforms are similar to dunes and antidunes[32]. Stability analyses also assumes so-called dune-covered

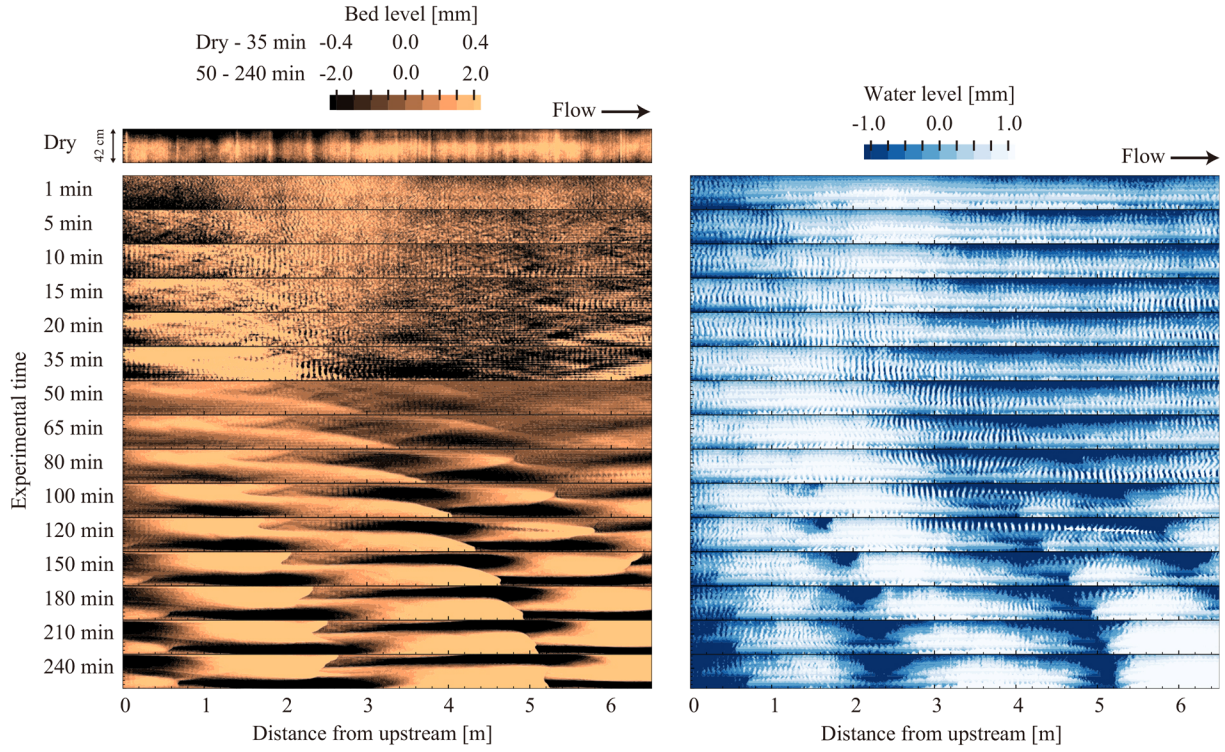

FIG. 3. Plane view of the dry bed level, the bed level and water level measured by ST under the condition of Member 1 in Case 2. The horizontal axis is the distance from the upstream of the measurement section. The vertical axis is the distance from the right bank. The coloring range of the bed level is different between Dry to 35 min and 50 min to 240 min from the beginning of the experiments.

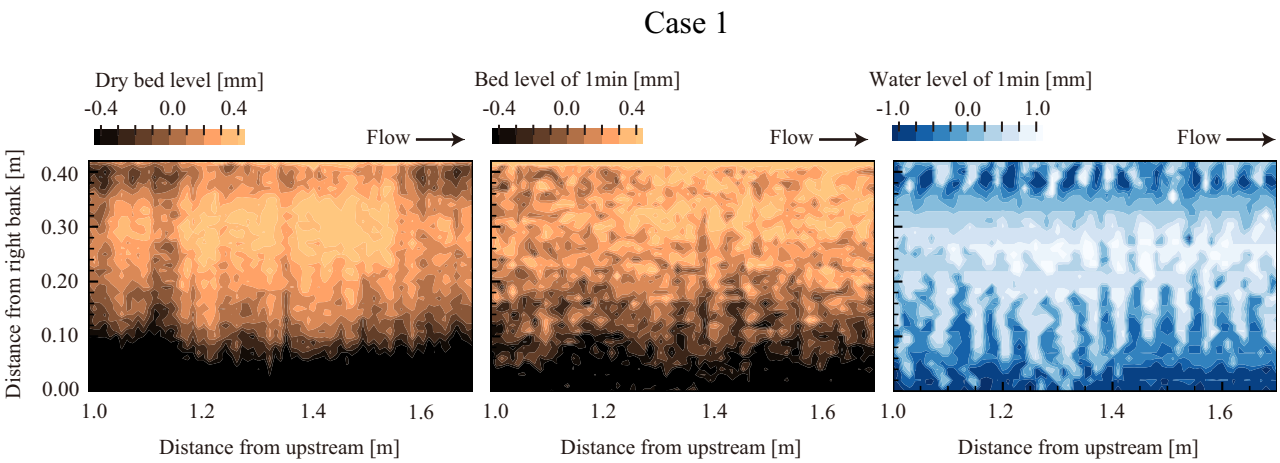

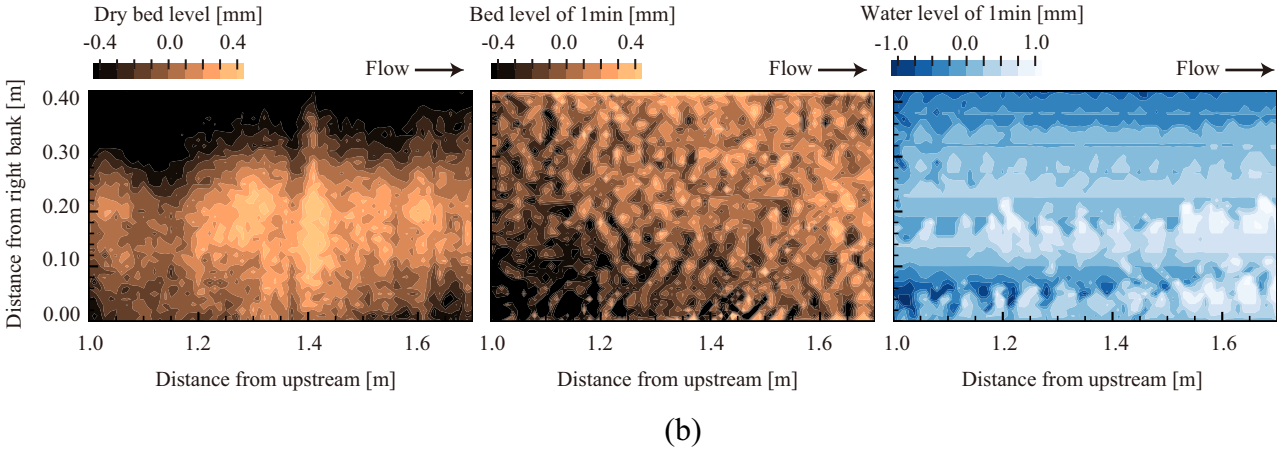

FIG. 4. From left to right, the dry bed level, the bed level and water level 1 minute from the beginning of the experiments.

beds[16–19,33,34] as the initial shape of the sandbar formation. The shapes of both the bottom surface and water surface are uniform in the transverse direction, and there appears to be a 2D shape. Bedforms that were a 2D shape transitioned over time to a 3D shape that obliquely intersected the channel. According to previous studies, oblique bedforms are similar to rhomboid bars[12]. Rhomboid bars grew in wavelength and height, eventually forming alternate bars. At the final stage of the experiments, in contrast to the early stage of the experiments, the wave height of the water surface is smaller than that of the bottom surface.

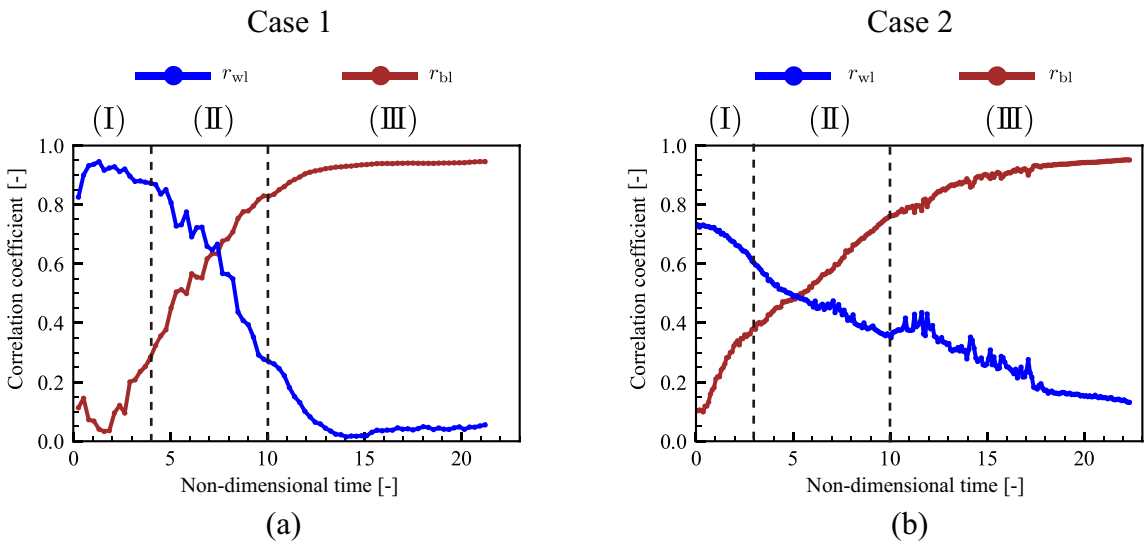

FIG. 5. Correlation coefficients between the water surface and flow depth and between the bottom surface and flow depth in each case. Correlation coefficients are absolute values. The horizontal axis is the dimensionless time. The black dotted line in each figure divides the occurrence and development process of sandbars into three phases.

2. *Correlation coefficients*

The method using correlation coefficients by Moteki *et al.*[26] makes it clear whether the water surface or the bottom surface contributes to the flow depth distribution at each stage of sandbars initiation and development. This method also classifies the process of sandbars formation into three phases. To obtain a more quantitative view of the forming process, the correlation coefficients were quantified for our measurement results.

Fig. 5 shows the results, where r_{wl} and r_{bl} are the correlation coefficients between the water surface and flow depth, and the bottom surface and flow depth, respectively, taking absolute values. The horizontal axis is the dimensionless time. The black dotted lines approximately divide the process of sandbars formation into three phases, based on a study by Moteki *et al.*[26]. These results are averaged over five measurements. The figures show that r_{wl} is large in Phase I, while r_{bl} is large in Phase III. This means that in Phase I, the wave height of the water surface waves is larger than that of the bedforms, and conversely, in Phase III, the wave height of the sandbars is larger than that of the water surface waves. These results are consistent with the qualitative discussion in the previous subsubsection.

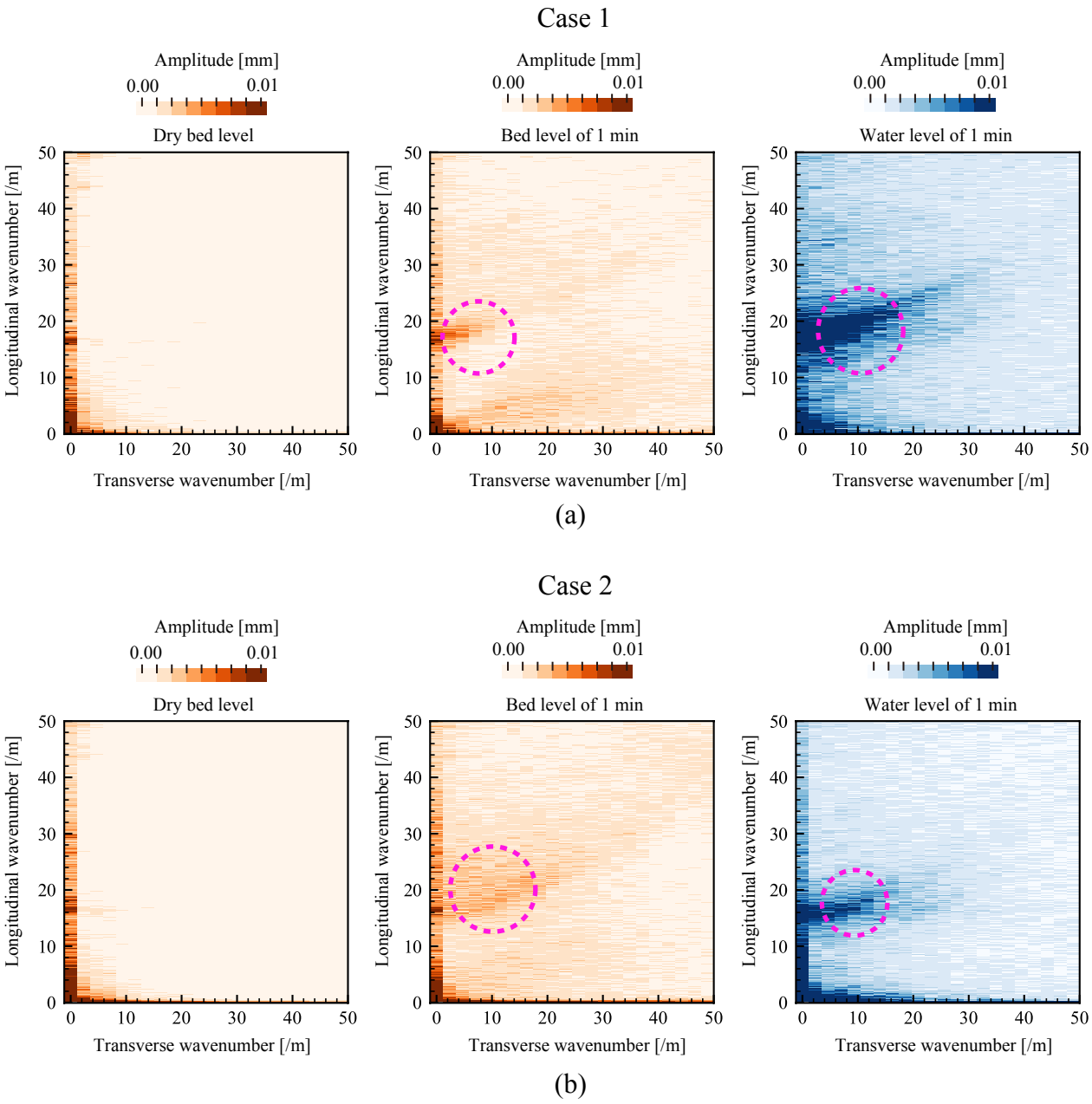

FIG. 6. Results of 2D wavenumber analysis. In each case, from left to right, the dry bed level, the bed level and water level 1 minute from the beginning of the experiments. Amplitudes of longitudinal and transverse wavenumbers are shown.

3. 2D wavenumber analysis

To quantify bedforms generation immediately from the beginning of the experiment, a 2D planar wavenumber analysis was performed for the dry bed, bottom surface and water surface 1

minute from the beginning of the experiments. The results of the analysis are shown in Fig. 6. The amplitudes are averaged over five measurements. The target sections are all shown dry and at 1 minute in Figs. 2 and 3. The figures show that there are almost no wavenumbers in the dry bed in both cases. In contrast, at 1 minute from the beginning of the experiments, the amplitude of the bottom surface is large in the area marked by the pink circle. The longitudinal wavenumber in the area is approximately 20 m^{-1}, which is approximately 5 cm in wavelength. The analysis of the water surface shows that amplitudes with the same wavenumber as the bedforms are dominant and are larger than those of the bedforms. These results are consistent with the results seen in the plane view of Fig. 4.

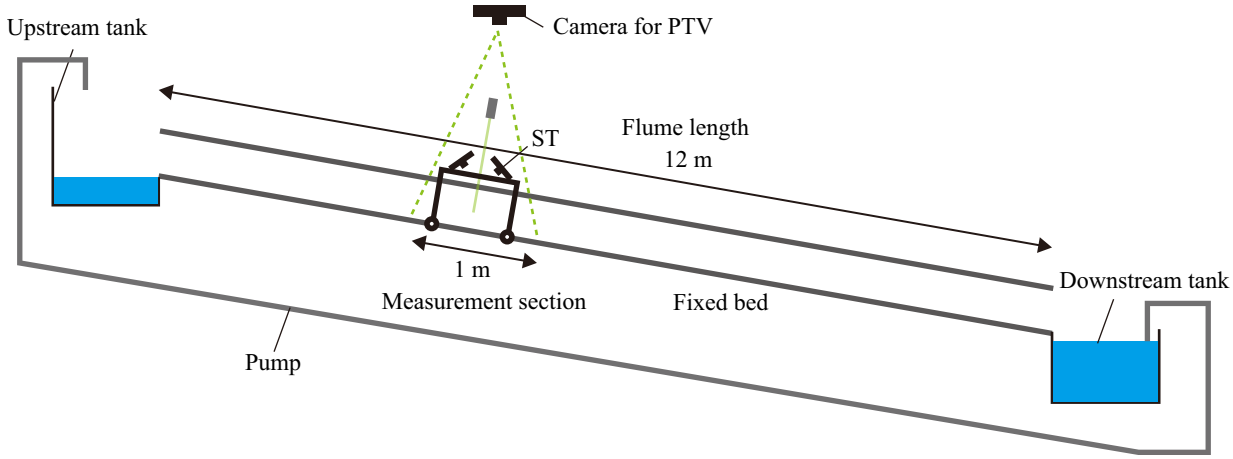

FIG. 7. Longitudinal view of the flume in the fixed-bed experiment.

III. FLUME EXPERIMENT ON THE FIXED BED

The results of the previous section showed that undulations on both the water surface and bottom surface already existed 1 minute from the beginning of the experiment. Since the amplitude of the water surface undulations was larger than that of the bottom undulations, the water surface undulations may have influenced the occurrence of the bottom undulations commonly called bedforms. At this point, however, it is unclear whether undulations occur on the water surface first. Clarifying this process has significant implications for revisiting the hypothesis on the occurrence of sandbars. In this section, we investigated the behavior of the water surface undulations in fixed-bed channel.

A. Measurement method

The channel used for the fixed-bed experiment is shown in Fig. 7. The same flume used in the previous section was used, but as mentioned above, the bottom was not covered with sand and was a fixed smooth surface. The geometry of the water surface was measured by ST as in the previous experiments, and surface flow velocities were measured by a simple particle tracking velocimetry (PTV) technique because it is necessary to investigate the mechanism of occurrence from multiple angles, accounting for not only the shape but also the flow velocities. This PTV method and its accuracy are outlined in Appendix A.

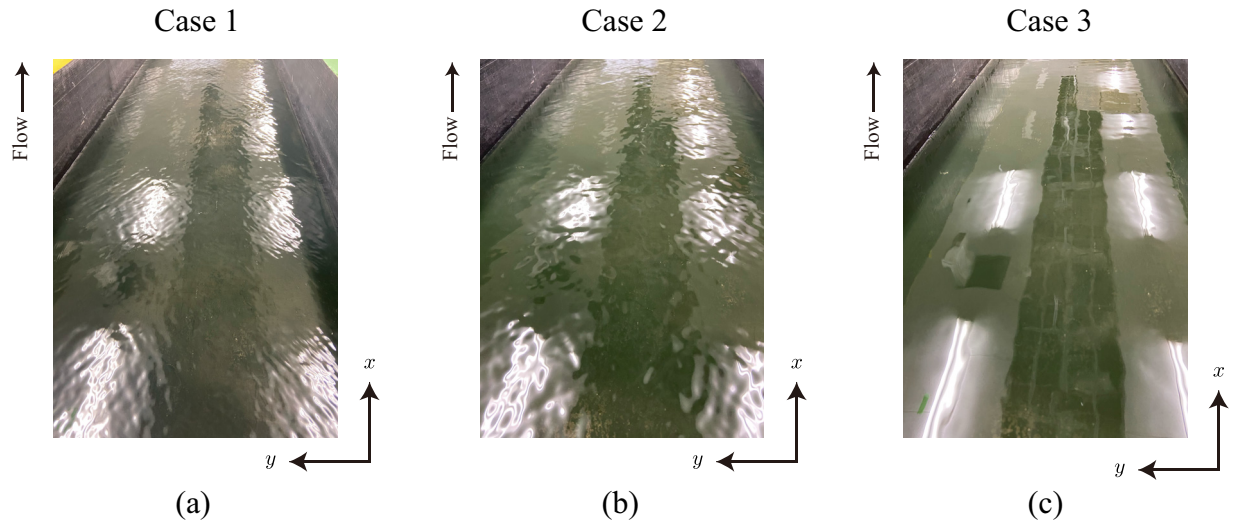

FIG. 8. Photographs of the water surface shape for each case in the fixed-bed experiments. The flow is in the upward direction in this paper.

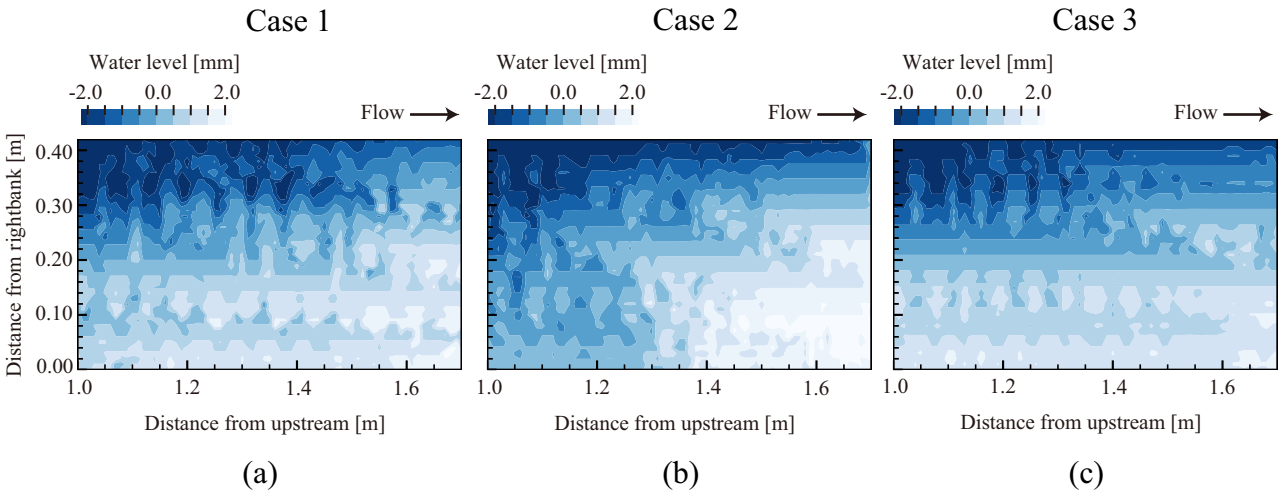

FIG. 9. Plane view of the water surface measured by ST for each case in the fixed-bed experiments. The measurement section for these figures is the same as that in Fig. 8.

B. Results

1. Water surface on the fixed bed

Figs. 8a and 8b show photographs of the water surface under the conditions described in the previous subsection. The photographs show that intersecting patterns on the water surface fully covered whole of the channel in both cases, even though the bed surface is a smooth. The heights

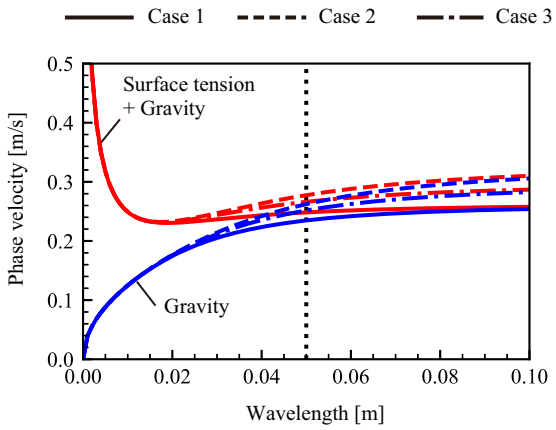

FIG. 10. Relation between phase speed and wavelength of water surface waves in the fixed-bed experiments from Eq. 7. The red lines take into account the effects of surface tension and gravity. The blue lines take into account the effect of gravity only. The black dotted line is the wavelengths of the water surface waves measured by ST.

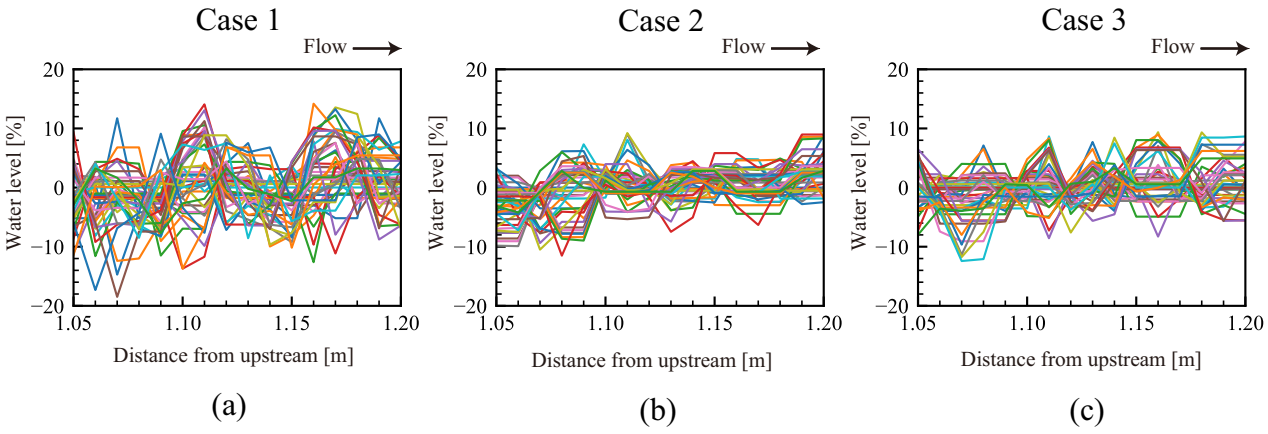

FIG. 11. Longitudinal view of the water surface measured by ST for each case in the fixed-bed experiments. Color-coded for each cross section.

of the patterns are larger in Case 1 than in Case 2. Although the water surface appears to be irregular, the water surface is hardly moving and seems to be standing waves. We also visually confirmed that the patterns were present in the flume outside the photographed area.

Figs. 9a and 9b show the measurement results of the water surface measured by ST. The figures showed that waves with a wavelength of approximately 5 cm and a height of several millimeters occur in both cases. These wavelengths and heights are generally consistent with the characteristics of the patterns observed on the water surface of the moving bed in Figs. 2 and 3.

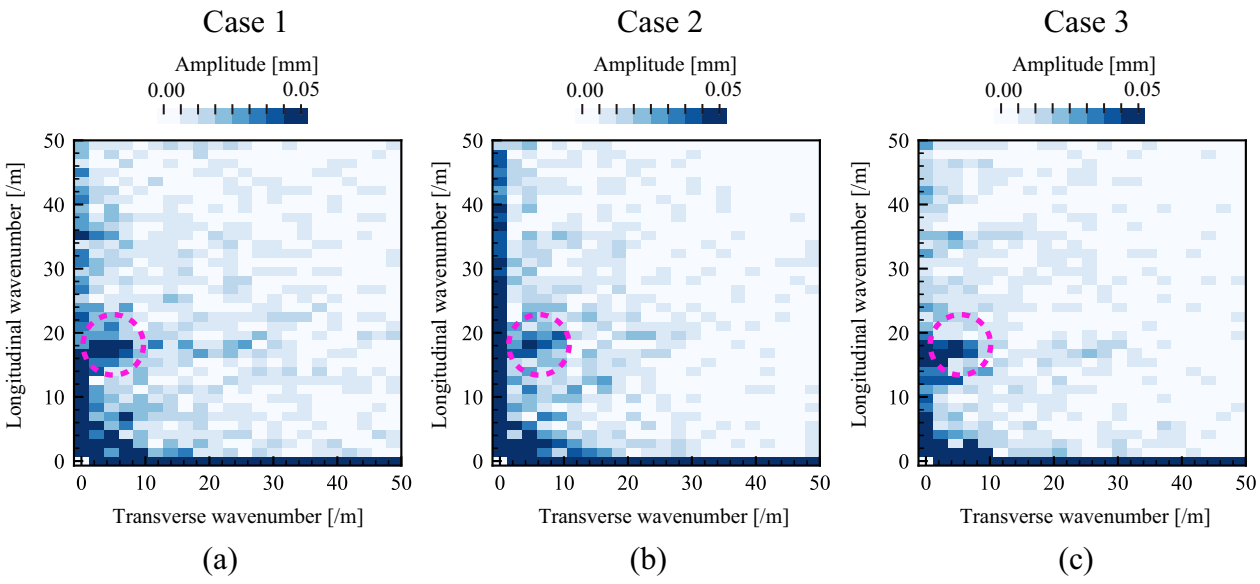

FIG. 12. Results of 2D wavenumber analysis for the water surface measured by ST for each case in the fixed-bed experiments. Amplitudes of longitudinal and transverse wavenumbers are shown.

To understand the nature of the standing waves with a wavelength of 5 cm in each case, we performed the following two approximate checks. First, the linear dispersion relation derived from the small amplitude waves theory (Airy's theory) was used as follows:

$$c = \pm\sqrt{\left(\frac{g}{k} + \frac{\tau}{\rho}k\right)\tanh(k\bar{h})}, \tag{7}$$

$$k = \frac{2\pi}{\lambda}, \tag{8}$$

where c is phase velocity, k is wavenumber, λ is wavelength, τ is surface tension coefficients, $\tau = 0.074$ N/m, ρ is density of water, $\rho = 1000$ kg/m^3, $\bar{h}$ is mean flow depth. The first term means gravity effect and the second term means surface tension effect. In Case 1, $\bar{h} = 0.7$ cm, $\lambda = 5$ cm were substituted. In Case 2, $\bar{h} = 1.1$ cm, $\lambda = 5$ cm were substituted. These mean flow depths were simply measured with a ruler. Fig. 10 shows that these waves can ignore the effects of surface tension. Second, depth-to-wavelength ratio $\bar{h}/\lambda$ in Case 1 is 1.1/5 and in Case2 is 0.7/5; these gravity waves are generally classified as shallow-water waves located in the middle of wave classification. Those results indicate that the effects of the wave reaches to the bottom.

Figs. 11a and 11b show the longitudinal cross sections of Figs. 9a and 9b. The water level is nondimensionalized by $\bar{h}$. The number of cross sections is 43 in the channel width direction. The range of the figure is limited to the area not affected by the slight tilt of the measured plane view

in the longitudinal direction. It is clear that the maximum amplitude in Case 1 is approximately 20 % of $\bar{h}$ and that the maximum amplitude in Case 2 is approximately 10 % of $\bar{h}$. Fig. 12 shows the result for the 2D wavenumber analysis of the water level, as in the previous section. The figure shows that the longitudinal wavenumber of 20 m^{-1} is dominant.

2. Flow velocity on the fixed bed

The first and second rows of Figs. 13a and 13b show the longitudinal component u of the surface flow velocity and the ratio v/u of the transverse component v to u measured by PTV, respectively, on the 1 cm mesh plane. The discontinuously small value near the center of u is due to the unevenness of the black coating of the channel. The reason for the slightly nonuniform bias observed in u across the cross section may be the slight slope of the channel. The plane view displays the channel at a width of 70 cm and a length of 35 cm due to the limitation of the angle of view. The Froude number F was calculated to be 1.62 in Case 1 and 1.09 in Case 2 using following equaiton:

$$F = \frac{\bar{u}^{3/2}}{\sqrt{g\frac{Q}{B}}}, \tag{9}$$

where $\bar{u}$ is the area mean value of u. The number of data points N obtained from PTV varies depending on the mesh, as shown in the third rows of Figs. 13a and 13b. u and v/u are the mean values of the data obtained per mesh. The fourth row of the same figure shows the standard deviation σ of the composite flow velocity V of u and v in the mesh. σ is divided by the area mean of V. The figures show that the maximum N is 1000 in Case 1 and Case 2, and σ is less than 10 % in most regions.

In the u value of Case 1, the intersecting patterns, also seen in Fig. 8a, are existed. The same intersecting patterns were observed in v/u. In the u value of Case 2, the waves with a wavelength of approximately 5 cm are observed, similar to those observed by ST. In contrast, they were not observed in v/u.

As in the previous subsubsection, Figs. 14a and 14b show longitudinal plots of the dimensionless values of u with $\bar{u}$. The display area is the white dotted line on the contour of u for each condition in Figs. 13a and 13b to remove restrictions such as missing measurements. These figures show that the maximum amplitudes ranged from 2 to 3 % in both cases.

Figs. 15a and 15b show the results of the wavenumber analysis of u. The analysis area is the

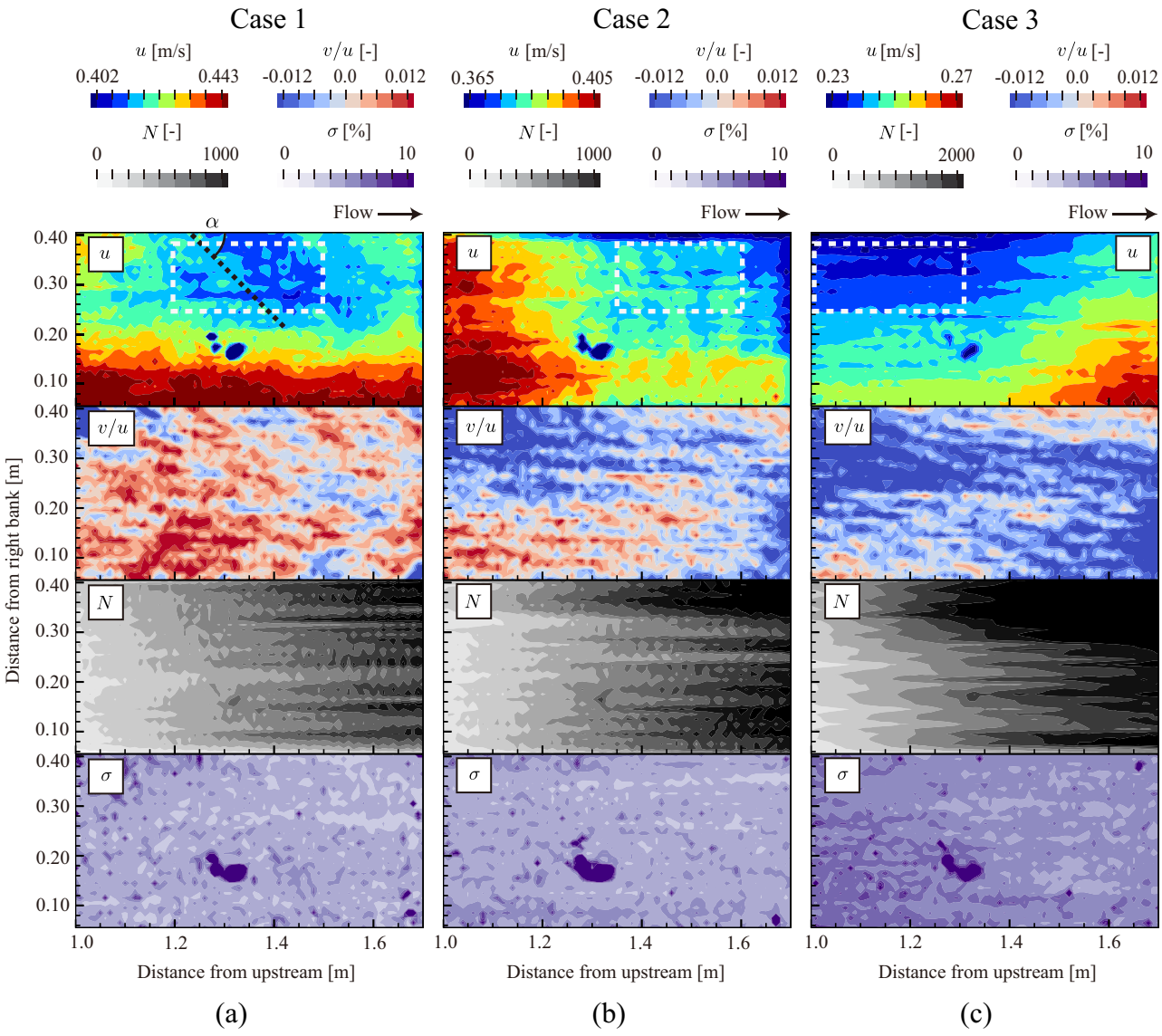

FIG. 13. Plane view of surface flow velocity measured by PTV for each case in the fixed-bed experiments. From the top, longitudinal flow velocity, transverse per longitudinal flow velocity, number of data points per mesh, and standard deviation of composite flow velocity. The black dotted line is the reference line used to measure the angle of the standing waves with the sidewall. The section surrounded by the white dotted line is the wavenumber analysis section.

same as in Fig. 14 and is within the white dotted line on the u of Fig. 13. In Case 1, the white circles in the figure show the predominance of longitudinal wavenumbers below 10 m^{-1}. These wavenumbers are correspond to the intersecting patterns. In Case 2, the white circles in the figure show the predominance of longitudinal wavenumbers below 20 m^{-1}. The results are consistent with those seen in the plane view.

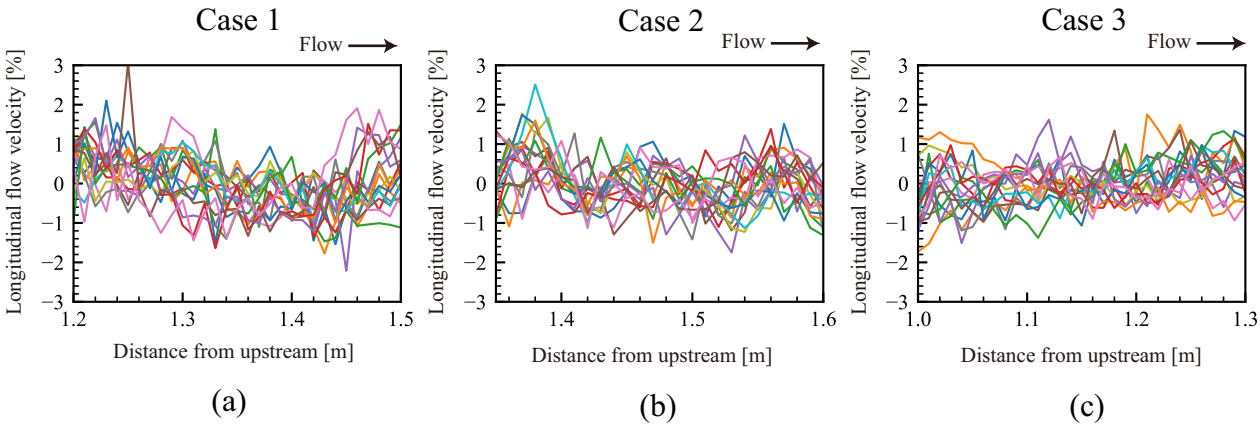

FIG. 14. Longitudinal view of surface flow velocity measured by PTV for each case in the fixed-bed experiments. Color-coded for each cross section.

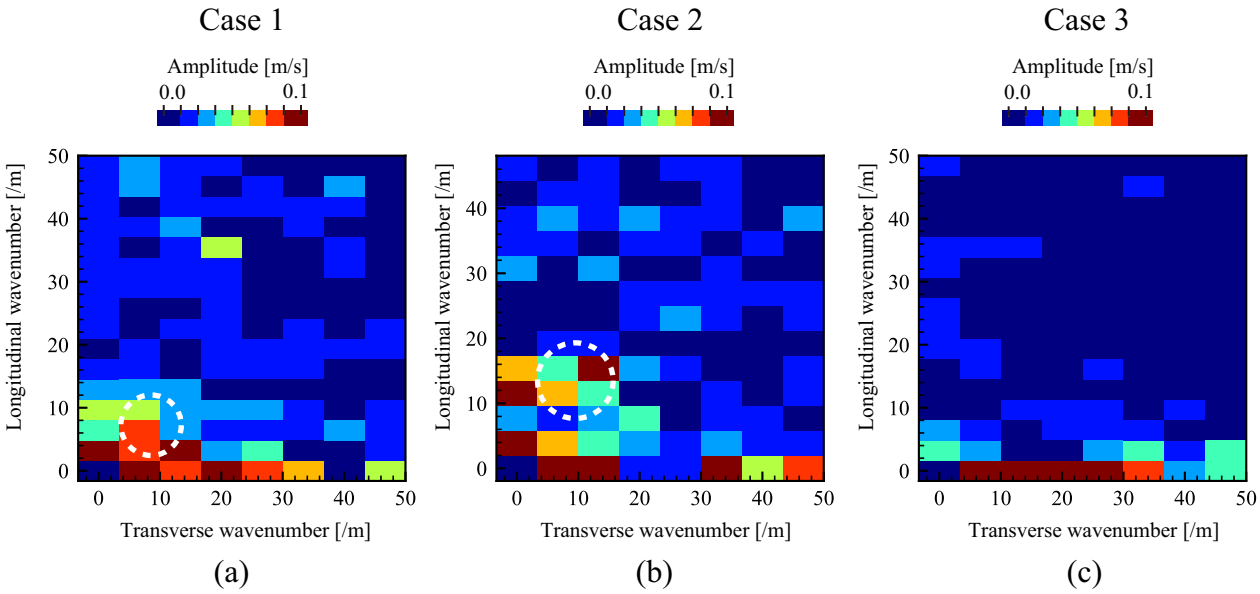

FIG. 15. Results of 2D wavenumber analysis for longitudinal surface flow velocity measured by PTV for each case in the fixed-bed experiments. Amplitudes of longitudinal and transverse wavenumbers are shown.

In this section, the experimental results show that the water surface had intersecting patterns similar to standing waves before bedforms occur where $\beta > \beta_c$. This result could renew the conventional hypothesis on the occurrence of sandbars.

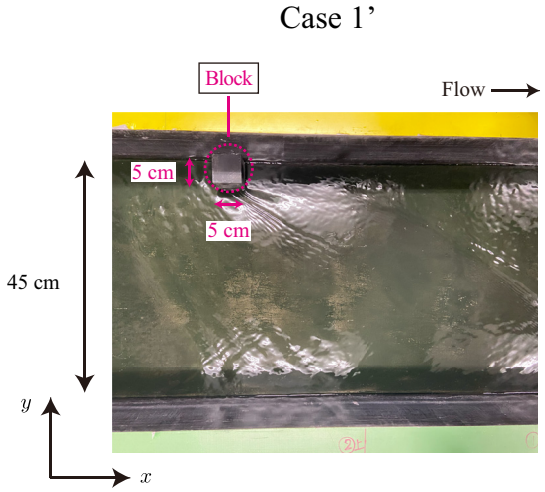

FIG. 16. Photograph of a block placed along the left sidewall under the conditions of Case 1' by flowing water through it. The block is a cube with 5 cm long sides.

IV. DISCUSSION

A. What causes intersecting patterns?

Here we clarify why the intersecting patterns occurs despite a flat bottom. Some obstacle in the sidewalls or inside the channel in supercritical flow generate shock waves[35]. If the wave angles are the same with and without obstacle, the intersecting patterns are most likely to be shock waves and caused by the sidewalls. We intentionally generated waves by placing obstacles in the channel and measured the angle it made with the sidewall.

A cube with 5 cm long sides was placed along the left sidewall, as shown in Fig. 16. Surface flow velocities were captured by PTV as shown in Fig. 17. The hydraulic conditions for this experiment are the same as those for Case 1, but we refer to it here as Case 1'. Figs. 16 and 17 show that waves are generated from the block.

The angles of the waves to the sidewalls were compared with and without the block, referring to the black dotted lines in Figs. 13 and 17. Since it was difficult to find the reference line from u in Fig. 17, we used the line where the positive and negative values just switch in v/u as the reference line. In both Case 1 and Case 1', the angles α of the reference line to the sidewall were generally consistent at 45 degrees. This result indicates that the intersecting patterns may have the same characteristics as those generated when an obstacle is placed. However, the following points are questionable. The angle that shock waves make with the sidewall is theoretically described by

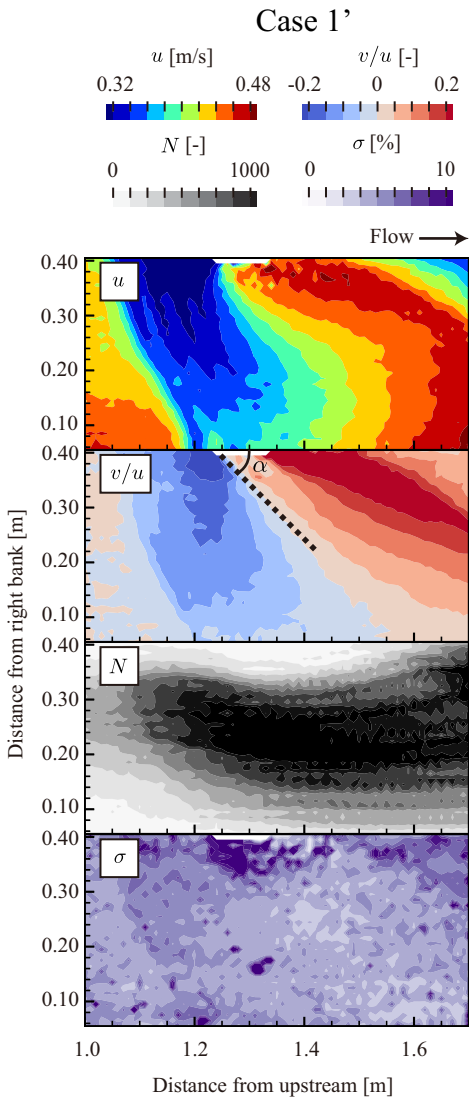

FIG. 17. Plane view of the surface flow velocity measured by PTV when the block was placed along the left sidewall and then flowed under the conditions of Case 1'. From the top, longitudinal flow velocity, transverse per longitudinal flow velocity, number of data points per mesh, and standard deviation of composite flow velocity. The black dotted line is the reference line used to measure the angle of the wave with the sidewall.

the following equation[13]

$$\alpha = \arcsin\left(\frac{1}{F}\right). \tag{10}$$

Substituting $F = 1.62$ in Case 1 into the above equation yields 38 degrees. The angle is slightly sharper than the measured case. It remains to be seen what is responsible for this angle discrepancy.

Why do the intersecting patterns occur on the water surface even though the bottom surface is

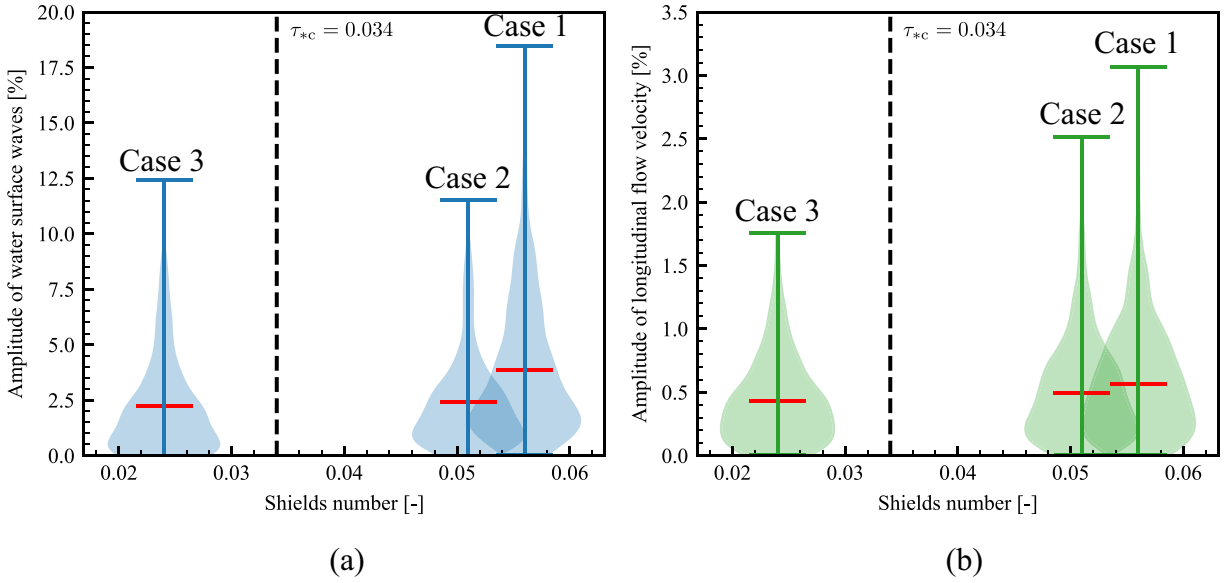

FIG. 18. The amplitudes of (a) water surface waves and (b) surface flow velocity profiles in Figs. 11 and 14 are shown as probability density functions for each condition. The red line is the mean value. The horizontal axis is the Shields number.

flat? We showed that the intersecting patterns covered the entire channel and seemed to generate from the sidewalls. We also showed that the pattern angles were approximately matched with and without the block. Moreover, in general, the planar distribution of the flow velocity is parabolic, with a smaller velocity near the sidewalls and a larger velocity near the center of the channel. Considering the above, we suppose that the intersecting patterns are generated by sidewalls, but we cannot go into further detail.

B. Can intersecting patterns occur on the water surface when $\tau_* < \tau_{*c}$?

We showed that the intersecting patterns on the water surface occurred on the smooth bed under sandbars forming conditions. The patterns initially occur on the water surface, and then the patterns led to occur bedforms, even under conditions in which sandbars do not form where $\beta < \beta_c$, under conditions in which sediment transport occurs where $\tau_* > \tau_{*c}$. However, it is unclear whether intersecting patterns occur under conditions whereby sediment transport cannot occur where $\tau_* < \tau_{*c}$.

We also investigated the behavior of water surfaces where $\tau_* < \tau_{*c}$, to provide a unified explanation for the process of sandbars formation. Case 3, in which sediment transport does not occur, was prepared and is shown in Table I. Under this condition, water surfaces were measured and analyzed as in the previous section. The results are shown in (c) of each figure in Fig. 8 to Fig. 15. From Eq. 9, the Froude number was calculated to be 0.83, which indicates subcritical flow.

Fig. 8c qualitatively shows that the flow is more stable in Case 3 than in Cases 1 and 2. Fig. 9c shows that flow appears to have less turbulence in the cross-sectional direction, but the waves occurred with a certain wave height in the longitudinal direction. These waves were stationary. Fig. 11c shows that the wave height in Case 3 is lower than in Case 1 but slightly higher than in Case 2. In Fig. 12c, the result of wavenumber analysis also shows that the wavenumber of approximately 20 m^{-1} has the same amplitude as that in Cases 1 and 2. We confirmed that the waves are gravity-dominated as shown in Fig. 10. The depth-to-wavelength ratio $\bar{h}/\lambda$ was 0.9/5, indicating that the waves were classified as shallow-water waves, as in Cases 1 and 2. On the other hand, Fig. 13c shows that there is no distribution of u and v/u corresponding to the waves. Fig. 15c also shows that there are no dominant wavenumbers. However, Fig. 14c shows that the wave height is approximately the same as in Case 2 when viewed as a percentage.

The above results were compared across conditions in Fig. 18. The figures quantify the scale of the wave height and flow velocity distribution of the water surface waves under the above conditions. The Shields number on the horizontal axis is calculated based on the measured values of the smooth surface condition. The Shields number is thus slightly smaller than the Shields number of the moving bed condition shown in Table I. Even under smooth surface conditions, however, τ_* exceeds τ_{*c} in Cases 1 and 2, and τ_* does not exceed τ_{*c} in Case 3. Whether the surface is smooth or rough is therefore not an essential issue when comparing the hydraulic conditions set up in this study for the Shields number.

The figure shows that there is no significant difference in the water surface whether τ_* exceeds τ_{*c} or not. In other words, the waves can occur on the water surface even when $\tau_* < \tau_{*c}$ with a similar magnitude as those observed under the condition of $\tau_* > \tau_{*c}$.

C. Proposal of a novel hypothesis on the inception of sandbars

We synthesize the results and then propose a novel hypothesis on the inception of sandbars. To avoid confusion, we define the water surface waves observed in the fixed-bed experiments as

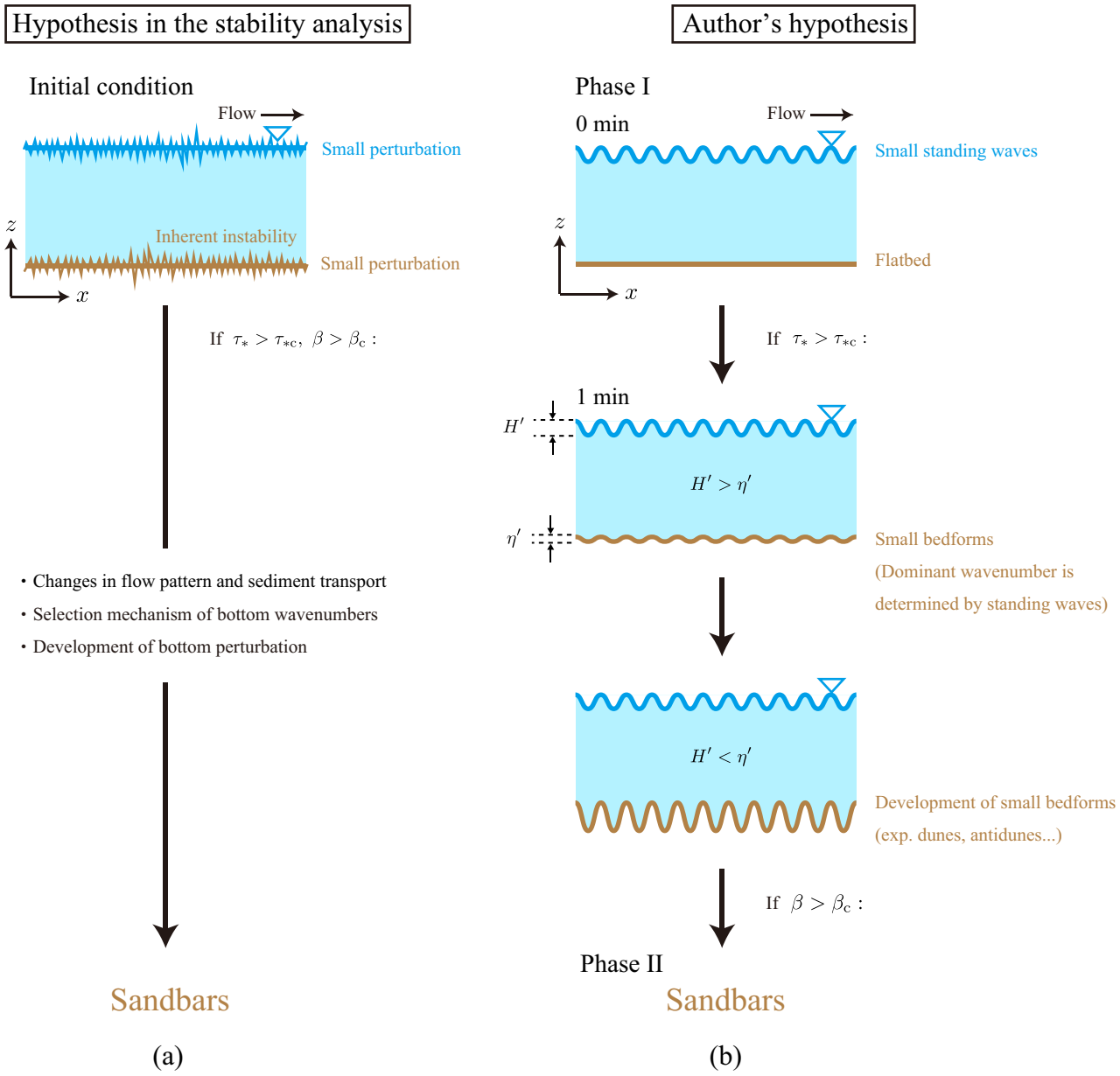

FIG. 19. (a) A conventional hypothesis on the occurrence of sandbars in the stability analysis, (b) Author's hypothesis on the occurrence of sandbars. H' is the wave height of water surface waves. η' is the wave height of bedforms.

"standing waves" and the bottom undulations with a wavelength of approximately 5 cm shown in Fig. 4 as "small bedforms". The results of this study are systematically presented as a schematic diagram on the right of Fig. 19. On the left of the figure, a schematic diagram is drawn based on the explanation for the occurrence of sandbars by Tubino, Repetto, and Zolezzi[17]. The fundamental difference between the two hypotheses is the primary surface that first deviates from a flat state:

whether it is the water surface or the bed surface. Theoretical analysis assumes that when $\beta > \beta_c$, the bottom becomes unstable, causing the flow to have a distribution. However, our measurement results showed that standing waves already existed before the occurrence of small bedforms. Our investigations also showed that when $\tau_* > \tau_{*c}$, the wavenumbers of small bedforms coincided with those of standing waves. This result indicates that the shape of the standing waves is projected onto that of small bedforms.

As can be seen from the photographs and PTV results, these standing waves are probably caused by the sidewalls. Sidewalls also physically confine water and sediment, and sandbars would not be formed without them[11,12,35]. In experimental flumes and straight river channels, sidewalls may contribute to the occurrence and development of sandbars.

Bedforms such as dunes and antidunes are expected to occur even under conditions where sandbars do not occur; therefore, it is appropriate to set the bifurcation point in the latter stage of Phase I to determine whether β exceeds β_c, as shown on the right of Fig. 19. Previous studies[17–19,33] have performed stability analyses considering not only flatbeds but also dune-covered beds as the initial bottom shape. Future works should conduct experiments under the $\beta < \beta_c$ condition to clarify the transition process to Phase II.

V. CONCLUSION

This study revisited a conventional hypothesis that assumes inherent instability on bottom is the inception of sandbars. We performed two different flume experiments. First, we conducted flume experiments on a moving bed that provided conditions for the development of sandbars. In the experiments, we measured both the water surface and bottom surface at high density and high frequency during the experiment. The results showed that sandbars do not form suddenly, but rather that small bedforms transition to rhomboid bars, and then the rhomboid bars transition to sandbars. The results of 2D wavenumber analysis showed that the dominant wavenumbers of the water surface and bottom surface agreed and that the amplitude of the water surface was larger. Second, we conducted fixed-bed experiments under the same conditions as a moving bed to ascertain the behavior of the water surface. The results of the fixed-bed experiments showed that standing waves were observed on the water surface even when the experimental conditions were steady and the flatbed channel was straight. A two-dimensional wavenumber analysis showed that the dominant wavenumbers of the standing waves and initial small bedforms were in good

agreement. We also suggested that the standing waves may originated from the sidewalls. The whole set of results indicated that standing waves were already present on the water surface before bedforms occurred. The standing waves on the water surface is one of the most prominent factors that lead to the occurrence of sandbars.

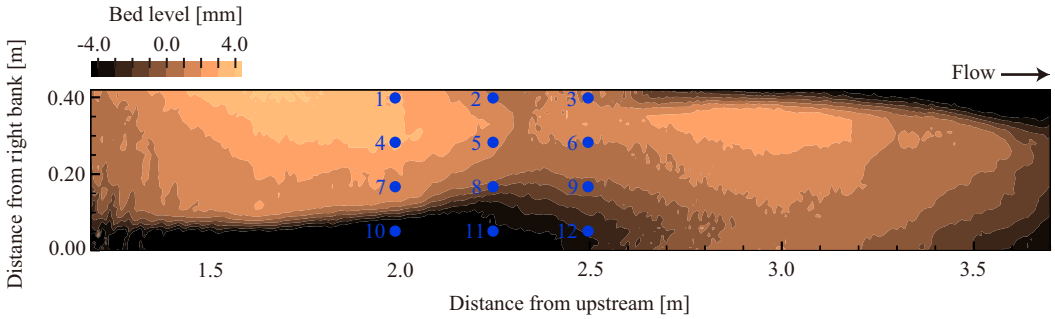

FIG. 20. Plane view of the sandbar model measured by ST. The points in the model are measurement points with an LDV.

Appendix A: Validation of flow velocity fields by PTV

1. Method

This section presents an overview of PTV measurements. The PTV measurements were made according to the following procedure. First, light tracers were sprayed on the water surface of the channel. Video images of the moving object were taken to obtain the tracer's position at each time point. Then, the surface flow velocity was calculated based on the tracer's distance traveled and the frame-per-second (fps) rate of the video. Styrofoam spheres with an average grain size of 2 mm were used as tracers. The specific gravity of the tracers was so low that they did not sink into the water during measurement. To record the tracer's moving bodies, the camera was placed 2 m directly above the flume, facing downward, and calibrated, with the resolution set to full HD (1920×1080) and the fps set to 40. In the video, a tracer is represented by 5×5 pixels, which is sufficient resolution to identify the feature of the particles during the particle tracking described below. During particle tracking, the 2D flow velocity field is obtained from the video using Optical Flow in OpenCV software[36].

2. Validation

Validation of the PTV-measured velocities was performed by comparing them with the velocities measured with laser Doppler velocimeter (LDV). Case 4 in Table I outlines the hydraulic conditions for the experiment. A model was created with fiber-reinforced plastic from the measured data of one wavelength of sandbars formed in the experiment on the moving bed. As shown

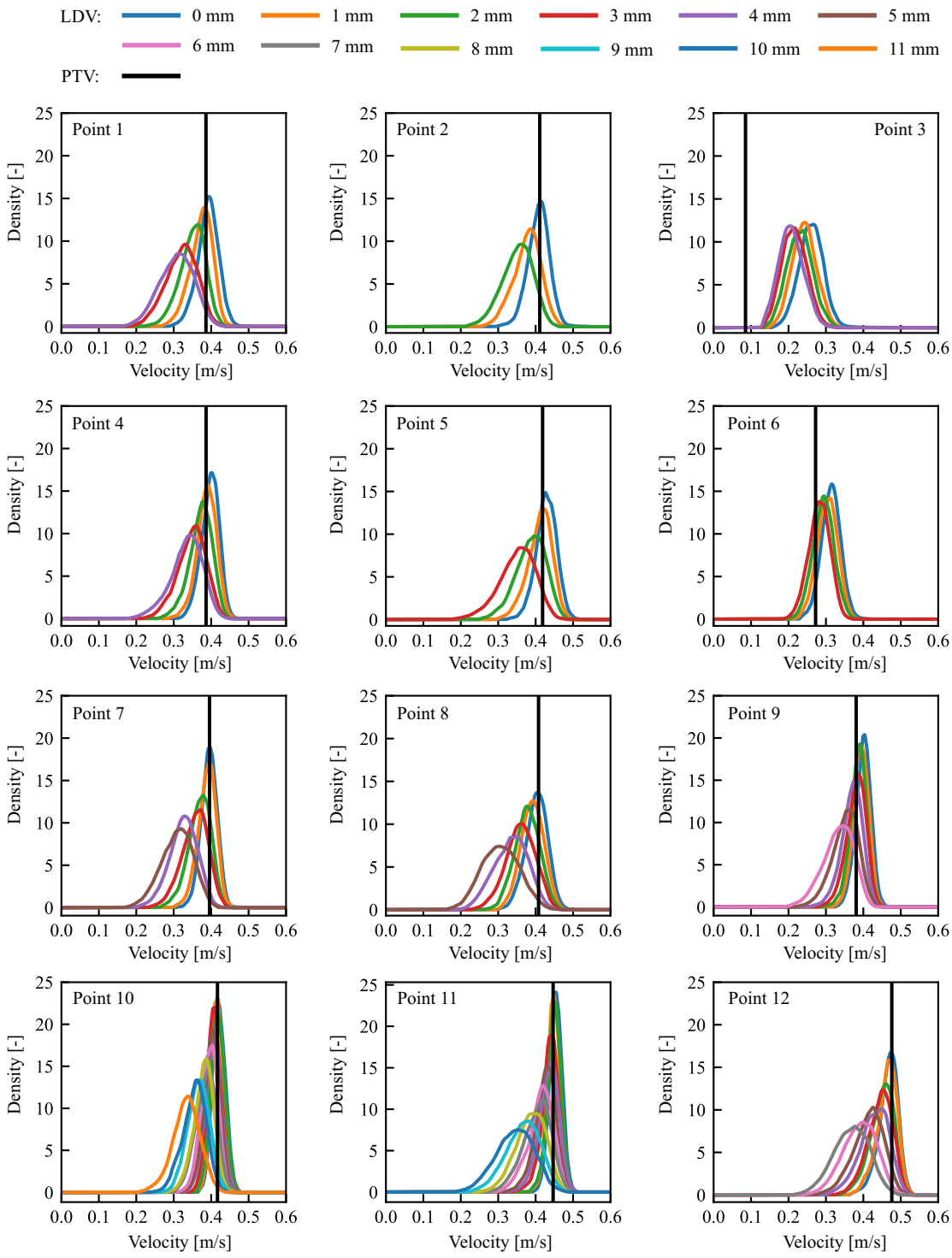

FIG. 21. Measurement results by PTV and with an LDV at each measurement point. Measurement results with an LDV are color-coded by flow depth and shown by the probability density function. The number of points measured with an LDV in the depth direction differs for each plane position. The black lines are values measured by PTV.

in Fig. 20, this is the fixed-bed condition with the model placed on the bottom of the channel. The twelve measurement positions were set up as shown in Fig. 20, and measurements with an LDV were conducted at intervals of 1 mm from the bottom surface to near the water surface at each position. More than 10,000 measurements were conducted at arbitrary plane positions and depths within the flow with an LDV to obtain a reliable flow velocity distribution for comparison. In the PTV measurements, tracers were sprayed until the number of flow velocity measurements at each measurement location reached several hundred, and the average of these measurements was obtained.

Fig. 21 shows the measurement results by PTV and with an LDV at each position. The figure shows that the surface flow velocity measured by PTV and the near-surface flow velocity measured with an LDV are different at the leading edge of the sandbar model, such as Point 3 and Point 6. The reason for the difference is likely the stepped flow at the leading edge of the sandbar model. In contrast, at other locations where flow fluctuations are relatively small, the two velocities are in good agreement. These results mean that the validity of PTV is sufficient, at least for near-uniform flow, as utilized in this study.

ACKNOWLEDGMENTS

We would like to thank AJE (https://secure.aje.com) for English language editing. We also thank T. Shioya and A. Suzuki for technical assistance with measurements by PTV and with an LDV.

DATA AVAILABILITY STATEMENT

The data that support the findings of this study are available from the corresponding author upon reasonable request.

REFERENCES

[1]B. Leopold, Luna and G. Wolman, M., "River channel patterns:braided,meandering and straight," *PHYSIOGRAPHIC AND HYDRAULIC STUDIES OF RIVERS* **282**, 39–85 (1957).

[2]G. M. Whitesides and B. A. Grzybowski, "Self-assembly at all scales," *Science* **295**, 2418–2421 (2002).

[3]R. Kinoshita, "Formation of "dunes" on river-bed -an observation on the condition of river meandering-," *Proceedings of the Japan Society of Civil Engineers*(in Japanese) **42**, 1–21 (1957).

[4]M. T. Ramirez and M. A. Allison, "Suspension of bed material over sand bars in the lower mississippi river and its implications for mississippi delta environmental restoration," *Journal of Geophysical Research: Earth Surface* **118**, 1085–1104 (2013).

[5]J. P. C. Eekhout, A. J. F. Hoitink, and E. Mosselman, "Field experiment on alternate bar development in a straight sand-bed stream," *Water Resources Research* **49**, 8357–8369 (2013).

[6]L. Adami, W. Bertoldi, and G. Zolezzi, "Multidecadal dynamics of alternate bars in the alpine rhine river," *Water Resources Research* **52**, 8938–8955 (2016).

[7]T. Branß, J. Aberle, and B. Hentschel, "Impacts on alternate bar geometry and dynamics in a trained sand bed river," *Front. Water* **4**, 1091872 (2023).

[8]S. Ikeda, "Prediction of alternate bar wavelength and height," *Journal of Hydraulic Engineering* **110**, 371–386 (1984).

[9]Y. Fujita and Y. Muramoto, "Studies on the process of development of alternate bars," *Bulletin of the Disaster Prevention Research Institute* **35**, 55–86 (1985).

[10]M. Ishihara and H. Yasuda, "On the migrating speed of free alternate bars," *Journal of Geophysical Research: Earth Surface* **127** (2022), 10.1029/2021JF006485.

[11]R. Kinoshita, "Study on dune in experimental channel (1) conditions of dune formation," *Shinsabo*(in Japanese) **26**, 28–34 (1957).

[12]H. Ikeda, "Experiments on bedload transport,bed forms,and sedimentary structures using fine gravel in the 4-meter-wide flume," (1983).

[13]O. Devauchelle, L. Malverti, E. Lajeunesse, C. Josserand, P.-Y. Lagree, and F. Metivier, "Rhomboid beach pattern: A laboratory investigation," *Journal of Geophysical Research* **115**, F02017 (2010).

[14]M. Colombini and A. Stocchino, "Three-dimensional river bed forms," *Journal of Fluid Mechanics* **695**, 63–80 (2012).

[15]M. Kuroki and T. Kishi, "Regime criteria on bars and braids in alluvial straight channels," *Proceedings of the Japan Society of Civil Engineers* (in Japanese) **342**, 87–96 (1984).

[16]M. Colombini, G. Seminara, and M. Tubino, "Finite-amplitude alternate bars," *Journal of Fluid Mechanics* **181**, 213–232 (1987).

[17]M. Tubino, R. Repetto, and G. Zolezzi, "Free bars in rivers," *Journal of Hydraulic Research* **37**, 759–775 (1999).

[18]B. Federici and G. Seminara, "Effect of suspended load on sandbar instability," *Water Resources Research* **42** (2006), 10.1029/2005WR004399.

[19]M. B. Bertagni and C. Camporeale, "Finite amplitude of free alternate bars with suspended load," *Water Resources Research* **54**, 9759–9773 (2018).

[20]M. Redolfi, "Free alternate bars in rivers: Key physical mechanisms and simple formation criterion," *Water Resources Research* **57**, e2021WR030617 (2021).

[21]J. Fredsøe, "Meandering and braiding of rivers," *Journal of Fluid Mechanics* **84**, 609–624 (1978).

[22]Y. Shimizu and T. Itakura, "Calculation of bed variation in alluvial channels," *Journal of Hydraulic Engineering* **115**, 367–384 (1989).

[23]A. Defina, "Numerical experiments on bar growth," *Water Resources Research* **39**, 1092 (2003).

[24]Y. Shimizu, J. Nelson, K. Ferrel, Arnez, K. Asahi, S. Giri, T. Inoue, T. Iwasaki, C.-L. Jang, T. Kang, I. Kimura, T. Kyuka, J. Mishra, M. Nabi, S. Patsinghasanee, and S. Yamaguchi, "Advances in computational morphodynamics using the international river interface cooperative (iric) software," *Earth Surface Processes and Landforms* **45**, 11–37 (2019).

[25]T. Iwasaki, Y. Shimizu, and K. Ichiro, "Sensitivity of free bar morphology in rivers to secondary flow modeling: Linear stability analysis and numerical simulation," *Advances in Water Resources* **92**, 57–72 (2016).

[26]D. Moteki, S. Seki, S. Muramatsu, K. Hayasaka, and H. Yasuda, "On the occurrence of sandbars," *Physics of Fluids* **35**, 016608 (2023).

[27]A. Crosato and E. Mosselman, "An integrated review of river bars for engineering, management and transdisciplinary research," *Water* **12** (2020), 10.3390/w12020596.

[28]E. Mosselman, "Studies on river training," *Water* **12** (2020), 10.3390/w12113100.

[29]D. Moteki, T. Murai, T. Hoshino, H. Yasuda, S. Muramatsu, and K. Hayasaka, "Capture method for digital twin of formation processes of sand bars," *Physics of Fluids* **34**, 034117 (2022).

[30]E. Meyer-Peter and R. Müller, "Formulas for bed-load transport," *2nd Meeting of International Association for Hydraulic Research, Stockholm* , 39–64 (1948).

[31]Y. Iwagaki, "(i) hydrodynamical study on critical tractive force," *Transactions of the Japan Society of Civil Engineers*(in Japanese) **41**, 1–21 (1956).

[32]T. Inoue, Y. Watanabe, T. Iwasaki, and J. Otsuka, "Three-dimensional antidunes coexisting with alternate bars," *Earth Surface Processes and Landforms* **45**, 2897–2911 (2020).

[33]R. Schielen, A. Doelman, and H. E. Swart, "On the nonlinear dynamics of free bars in straight channels," *Journal of Fluid Mechanics* **252**, 325–356 (1993).

[34]S. Lanzoni, "Experiments on bar formation in a straight flume: 1. uniform sediment," *Water Resources Research* **36**, 3337–3350 (2000).

[35]S. Fukuoka, T. Nakamura, K. Abe, and M. Igarashi, "Hydraulic roles of side banks in alluvial strean," *Proceedings of the Japanese Conference on Hydraulics*(in Japanese) **27**, 681–688 (1983).

[36]OpenCV, `https://opencv.org`